


 Cite this: *RSC Adv.*, 2021, **11**, 17332

## Synergy ascension of SnS/MoS<sub>2</sub> binary metal sulfides on initial coulombic efficiency and stable capacity for lithium storage†

 Kai Pan,<sup>a</sup> Yanna Sun,<sup>c</sup> Xingcun He,<sup>b</sup> Feiyan Lai,<sup>b</sup> Hongqiang Wang,<sup>c</sup> Libo Liang,<sup>b</sup> Qingyu Li,<sup>c</sup> Xiaohui Zhang<sup>c</sup> <sup>\*bc</sup> and Hongbing Ji<sup>a</sup>

Numerous efforts have been devoted to capability improvement and cycling stability in the past decades, and these performances have been significantly enhanced. Low initial coulombic efficiency is still a problem in the metal sulfide-based anode materials. This study developed a strategy to achieve high initial coulombic efficiency and superior capacity retention by interpenetrating binary metal sulfides of SnS and MoS<sub>2</sub> in a conductive carbon matrix. The synergy ascension of electrochemical performances for the metal sulfides is attributed to their mutual impeding effects on coarsening of metal grains and the capsule-shaped coating structure embedded in the carbon sheet architecture. The SnS/MoS<sub>2</sub>/C composite was prepared by a simple NaCl template-assisted ball milling method, and showed excellent electrochemical performances in terms of a high initial coulombic efficiency up to 90.2% and highly stable reversibility with a specific capacity of 515.4 mA h g<sup>-1</sup> after 300 cycles at 1.0 A g<sup>-1</sup>. All of these characteristics suggest that the proposed materials are superior among the previously reported metal sulfide-based anode materials for lithium-ion batteries.

Received 16th February 2021

Accepted 22nd April 2021

DOI: 10.1039/d1ra01267c

rsc.li/rsc-advances

### 1. Introduction

With the rapid demand of energy, the capacity of commercial graphite materials limits their application as anode materials for a new generation of high energy density lithium-ion batteries (LIBs).<sup>1–5</sup> It is necessary to develop new anode materials with high reversible capacity, rate capacity and cycling performance.<sup>6–10</sup> The anode performance has a significant effect on the overall energy and power density of the full batteries.<sup>11–13</sup> Considerable attention has been paid to metal sulfides, such as MoS<sub>2</sub> and Sn-based sulfides,<sup>14–16</sup> which have been considered as promising alternative anode materials due to their high theoretical capacity.<sup>17–19</sup> MoS<sub>2</sub> has attracted considerable attention because of its good chemical stability, high specific capacity as well as simple synthesis. However, volume change caused by phase transformation results in electrode pulverization in the cycling process, and the long-chain lithium polysulfide dissolving and moving to the anode would also lead to capacity loss.<sup>20–22</sup> With weaker Sn–S bond and larger interlayer spacing in

the layered structure, Sn sulfides are considered to have better kinetical characteristics of lithiation/delithiation compared to Sn oxides.<sup>23–26</sup> Studies have shown that a smaller volume change makes SnS more suitable for lithium storage than SnS<sub>2</sub>,<sup>27,28</sup> and it has also attracted interest in research fields of photocatalysis and photodetectors due to its superior physical and chemical properties.<sup>29–33</sup> However, the serious pulverization and low electronic conductivity also lead to fast capacity decay.<sup>34</sup>

Numerous effective strategies are introduced to improve the electrochemical performances of metal sulfides, such as reducing the particle size, designing special morphology, and embedding nanoparticles into conductive carbon matrices.<sup>35–39</sup> However, as a promising anode material candidate to replace the commercial graphite materials, the enhanced rate and cycling capability still cannot be applied in practice due to another key issue of the low initial coulombic efficiency (ICE). Although some effective efforts have been made to other metal-based anode materials, relatively few studies have reported effective strategies to achieve a high ICE for the metal sulfides.<sup>40–44</sup> Recently, Hu *et al.* have revealed that the coarsening of Sn phases led to a limited conversion back into SnO<sub>2</sub> during Li extraction, and the reversible capacity decreased with the increase in the cycling numbers. However, the high-density grain boundary among nanosized SnO<sub>2</sub> could suppress the Sn coarsening and enable high ICES (86.2–95.5%). In view of this, they inhibited the grain coarsening with transition metals to achieve a highly reversible conversion reaction, and all SnO<sub>2</sub>–

<sup>a</sup>School of Chemistry and Chemical Engineering, Guangxi Key Laboratory of Petrochemical Resource Processing and Process Intensification Technology, Guangxi University, Nanning 530004, China

<sup>b</sup>College of Materials and Environmental Engineering, Hezhou University, Hezhou 542899, China. E-mail: zxhui017@163.com

<sup>c</sup>Guangxi Key Laboratory of Low Carbon Energy Materials, Guangxi Normal University, Guilin 541004, China

† Electronic supplementary information (ESI) available. See DOI: 10.1039/d1ra01267c



metal-graphite composites with different metals exhibited an excellent initial coulombic efficiency.<sup>45</sup>

Combining the existing theoretical achievements, herein, this study introduces a strategy by interpenetrating binary metal sulfides of SnS and MoS<sub>2</sub> together in a conductive carbon sheet architecture *via* a salt template-assisted ball milling method. Such a unique binary metal sulfide aggregate embedded in a carbon capsule well suppressed the volume change upon cycling and promoted the transferring kinetics of charges. More importantly, the heterogeneous crystal phases with rich boundaries mutually impeded the coarsening of Sn and Mo grains produced in the electrode reaction. Furthermore, Mo catalyzed the decomposition of Li<sub>2</sub>O due to a much lower energy barrier, resulting in an enhanced reversibility of conversion reactions in the charge process. The synergistic effects achieved a high initial coulombic efficiency with superior retention capacity.

## 2. Experimental

### 2.1 Synthesis of SnS/MoS<sub>2</sub>/C composites

Commercially available metallic Sn (99.9%, 1–3 Micron, Yfnano) powder, SnCl<sub>4</sub>·5H<sub>2</sub>O, Na<sub>2</sub>MoO<sub>4</sub>·2H<sub>2</sub>O, NH<sub>2</sub>CSNH<sub>2</sub> and citric acid were used without further purification. SnS/MoS<sub>2</sub>/C was prepared by the NaCl template method with ball milling. In the first step, Sn powder (0.250 g), SnCl<sub>4</sub>·5H<sub>2</sub>O (0.366 g), Na<sub>2</sub>MoO<sub>4</sub>·2H<sub>2</sub>O (0.450 g), NH<sub>2</sub>CSNH<sub>2</sub> (0.846 g), citric acid (3.0 g), NaCl (25.0 g) and ID water (10.0 g) were placed in a 100 mL sealed stainless-steel jar with 30 g of stainless-steel balls. The milling speed was set as 500 rpm for 20 h. Then, the hybrids were dried at 80 °C and calcined at 450 and 750 °C for 2 h, respectively, under Ar atmosphere. NaCl particles were washed away from the black solid power by ID water, and the sample could be obtained after drying at 80 °C overnight. In addition, the reference sample of the SnS/C composite was prepared using 0.250 g of Sn power, 0.366 g of SnCl<sub>4</sub>·5H<sub>2</sub>O, 0.146 g NH<sub>2</sub>CSNH<sub>2</sub>, 3.0 g citric acid, 25 g NaCl and 10 g ID water under the same conditions, while MoS<sub>2</sub>/C was synthesized using 0.45 g Na<sub>2</sub>MoO<sub>4</sub>·2H<sub>2</sub>O, 0.70 g NH<sub>2</sub>CSNH<sub>2</sub>, 3.0 g citric acid, 25 g NaCl and 10 g H<sub>2</sub>O.

### 2.2 Materials characterization

General crystal structures of SnS/MoS<sub>2</sub>/C, SnS/C and MoS<sub>2</sub>/C were examined by X-ray diffraction (XRD, Rigaku D/max 2500) using Cu K $\alpha$  radiation from 10°–90° at a scanning rate of 10° min<sup>-1</sup>. The morphology of the composites was investigated using a field-emission scanning electron microscope (FE-SEM, JEOL 2011), and the morphology in detail was characterized by scanning and high-resolution transmission electron micrographs (TEM and HR-TEM, Philips FEI Quanta 200 FEG). X-ray photoelectron spectroscopy (XPS) was used to analyze the surface of the composites and chemical bonding. The thermal analysis of the carbon content was determined by TGA (TA Apparatus), in which the temperature was raised to 1000 °C at a rate of 5 °C min<sup>-1</sup> under air atmosphere.

### 2.3 Electrochemical measurements

The slurry for the electrode was fabricated from the as-prepared composites, Super-P and polymer binder (PVDF) in the weight ratio of 8 : 1 : 1 in a *N*-methyl-pyrrolidone solution. A Cu foil loaded with the formed slurry was dried at 80 °C overnight in an electric oven. The loading mass was about 0.4 mg cm<sup>-2</sup>. Then, the electrodes (SnS/MoS<sub>2</sub>/C, SnS/C and MoS<sub>2</sub>/C) were assessed by CR2025-type coin cells in an argon-filled glove box, composed of lithium metal as the counter electrode, Celgard (2340) as the separator and 1.0 M LiPF<sub>6</sub> in EC/EMC (1 : 1, vol%) as the electrolyte. All cells were aged for 12 h to ensure that the electrodes were completely soaked in the electrolyte. The electrochemical performances of the cells were assessed by a Land battery testing system (BT2013A). The cyclic voltammetry (CV) and electrochemical impedance spectroscopy (EIS) curves were recorded by an IM6 electrochemical workstation. The CV test was conducted in the voltage range between 0.01 V and 3 V, and the EIS measurements were implemented over the range from 0.01 Hz to 100 kHz.

## 3. Results and discussion

The preparation process of SnS/MoS<sub>2</sub>/C is shown in Fig. 1. In the first step, metallic Sn, Sn<sup>4+</sup> and MoO<sub>4</sub><sup>2-</sup> were thoroughly mixed, and refined in a citric acid solution medium under ball milling. After drying, the SnCl<sub>2</sub>–Na<sub>2</sub>MoO<sub>4</sub>·2H<sub>2</sub>O–NH<sub>2</sub>CSNH<sub>2</sub>–C<sub>6</sub>H<sub>8</sub>O<sub>7</sub> precursor coated the surface of the NaCl template particles with different sizes. Then, the Sn reacted with Sn<sup>4+</sup> to form Sn<sup>2+</sup> during a heat treatment under Ar atmosphere, in which the SnS and MoS<sub>2</sub> were synthesized, and citric acid was transformed to a carbon film on the NaCl particles. Finally, removing the template crystals left rich interspaces and pores in the architecture supported by the carbon film. For each carbon sheet, the large surface area offered increased electrochemically active sites for the SnS and MoS<sub>2</sub> composites.

The phase structures of the SnS/MoS<sub>2</sub>/C, SnS/C and MoS<sub>2</sub>/C composites were analyzed by XRD, as shown in Fig. 2A. The intensive peaks at 25.92°, 27.34°, 31.62° and 45.38° corresponding to the (120), (021), (111) and (002) planes observed in the patterns of the SnS/MoS<sub>2</sub>/C and SnS/C composites were ascribed to a highly crystalline structure of SnS (JCPDS no. 39-0354). The peaks at 14.40°, 39.52° and 49.82° can be attributed to (002), (103) and (105) planes of the hexagonal MoS<sub>2</sub> crystal structure (JCPDS no. 65-1951). The peak at 14.40° was indexed to the (002) plane of MoS<sub>2</sub>, which indicated the ordered stacking of S–Mo–S layers.<sup>46,47</sup> In addition, it is noted that the Sn/C composite contained a small amount of SnO<sub>2</sub> and Sn<sub>2</sub>O<sub>3</sub>, and the formed oxides could be contributed to the oxidation of Sn during ball milling and heat treatment. There were no peaks attributed to carbon, which may be due to a weak crystal structure caused by the relatively lower annealing temperature. The carbon structure in SnS/MoS<sub>2</sub>/C was evaluated by Raman spectroscopy, as shown in Fig. S1.† The characteristic peaks of carbon at around 1591.1 and 1348.4 cm<sup>-1</sup> correspond to the G and D bands. It is well known that the D band is assigned to the vibrations of carbon atoms with dangling bonds for the in-plane



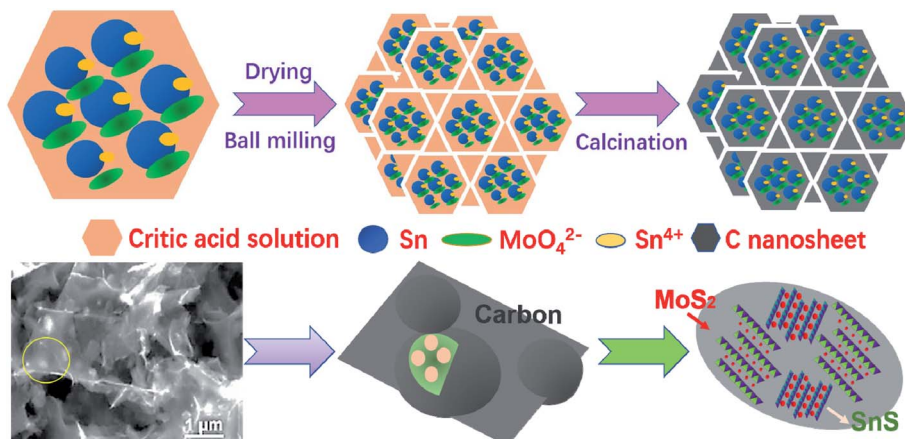


Fig. 1 Schematic of the fabrication process and the interpenetrated structure.

terminations of disordered graphite, and the G band is ascribed to the  $E_{2g}$  mode in the basal plane of crystalline graphite. Furthermore, there are another two peaks at around 377.0 and 403.4  $\text{cm}^{-1}$  due to the  $E2g^1$  and  $A_{1g}$  Raman modes of  $\text{MoS}_2$ , respectively. The composite is a typical carbonaceous material. The contents of C, SnS and  $\text{MoS}_2$  in the SnS/ $\text{MoS}_2$ /C composite were measured by inductively coupled plasma (ICP) and thermogravimetric analysis (TGA), as shown in Fig. 2B. The results showed that the mass percentage of Sn and Mo were 4.534 and 24.640 wt%, respectively. According to the TGA curves, the composite showed a weight loss of 34.58%. At the range of 100–400  $^{\circ}\text{C}$ , the weight change corresponded to the decomposition of carbon, oxidation of  $\text{MoS}_2$  to  $\text{MoO}_3$  and oxidation of SnS to  $\text{SnO}_2$ . As calculated by the result obtained from the ICP and TGA measurements, the contents of  $\text{MoS}_2$  and SnS were 71.34 and 3.69 wt%, respectively.

The composition of the SnS/ $\text{MoS}_2$ /C sample was explored by the XPS analysis, as shown Fig. 3. Fig. 3A shows a typical survey spectrum of the composite presenting the elements of Sn, Mo and S. Fig. 3B shows the high-resolution XPS spectrum of Sn 3d, and the two main peaks located at 486.9 and 495.3 eV correspond to Sn 3d<sub>5/2</sub> and Sn 3d<sub>3/2</sub>, respectively, which are ascribed

to the binding energy of  $\text{Sn}^{2+}$  in SnS. The peaks at 235.8 and 232.6 eV are assigned to Mo 3d<sub>3/2</sub> and that of Mo 3d<sub>5/2</sub> is located at 229.3 and 226.6 eV; the binding energy can be attributed to  $\text{Mo}^{4+}$  state. The high resolution of S 2p<sub>3/2</sub> at 169.1/168.3 eV and S 2p<sub>1/2</sub> at 163.3/162.1 eV are attributed to the binding energy of S in  $\text{MoS}_2$  and SnS.

The morphology of the SnS/ $\text{MoS}_2$ /C sample is shown in the SEM and TEM images in Fig. 4. Fig. 4A displays that the composite consisted of carbon nanosheets, and these staggered sheets support each other to form a three-dimensional grid. The cross-linked structure is beneficial for the electrode transport in the whole active material. The framework leaves rich pores and exposes large surface to the electrolyte, which promotes the transferring of ions from the electrode material to the electrolyte. From the magnification of the carbon sheets in Fig. 4B, the clear edge suggests an ultrathin sheet-like microstructure. Each particle is embedded in the carbon nanosheet and coated by the carbon layer as a capsule. The full coating protects the active material from the electrolyte and strengthens its structure stability along with cycling as well as improved conductivity. The carbon layer also impedes the particle aggregation of the active materials during heat treatment. By comparison, the SnS/

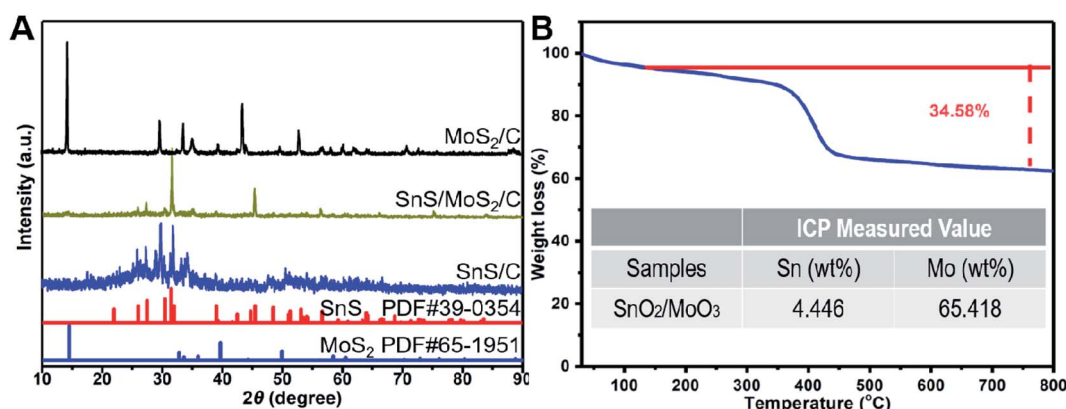


Fig. 2 XRD patterns of the SnS/ $\text{MoS}_2$ /C, SnS/C and  $\text{MoS}_2$ /C (A), TGA curve and ICP value of the SnS/ $\text{MoS}_2$ /C sample (B).



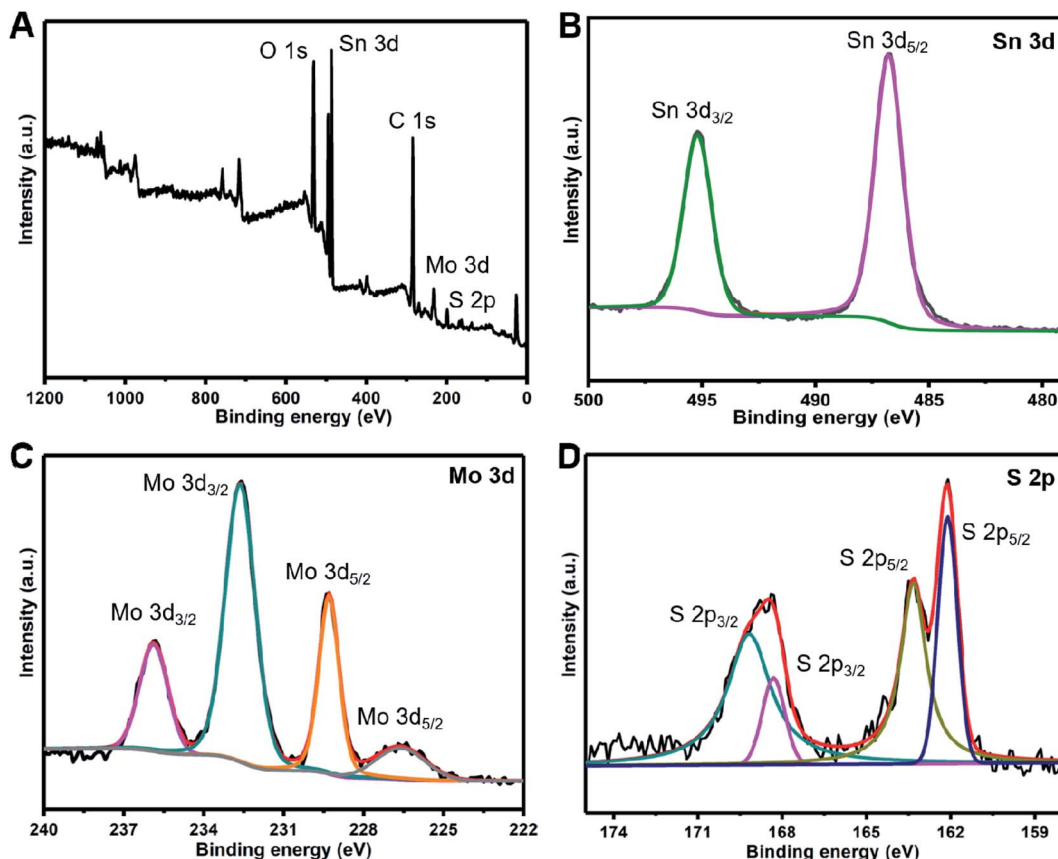


Fig. 3 The survey XPS spectra of the SnS/MoS<sub>2</sub>/C composite (A), the high resolution of Sn 3d (B), Mo 3d (C) and S 2p (D).

C and MoS<sub>2</sub>/C samples show a similar composite structure to SnS/MoS<sub>2</sub>/C (Fig. S2A and B†). The nitrogen adsorption-desorption analysis of the samples (Fig. S3A–C†) exhibits the typical characteristics of mesoporous materials with a BET surface area of 88.01 m<sup>2</sup> g<sup>-1</sup> for SnS/MoS<sub>2</sub>/C (Fig. S3C†). The corresponding pore size distribution (Fig. S3D†) indicates that the sample has an abundant mesoporous texture. The TEM image in Fig. 4C shows numerous nanoparticles are dispersedly embedded in the carbon sheets. The high dispersion of the active material is beneficial to capability and weakens the volume effects. To further explore the local crystal phase of the dispersed particles in the HRTEM image, the local grain shows a multi-crystal structure. By measuring the lattice fringes of the crystal phases in Fig. 4D, the fringes correspond to the characteristic lattice plane of SnS and MoS<sub>2</sub>, respectively. Further characterization by EDS mapping (Fig. S2C†) also reveals the uniform interspersion of Sn, S and Mo elements in the carbon sheets. Therefore, the metal sulfides of SnS and MoS<sub>2</sub> were interpenetrated to form partial binary aggregates embedded in carbon capsules. The mutually impeding structure offers rich boundaries and then suppresses the coarsening of Sn and Mo grains. In addition, the Mo formed after lithiation tends to catalyze the decomposition of Li<sub>2</sub>O, which enhances reversibility of the conversion reactions in the charging process.

Fig. 5A shows the discharge-charge profiles of the as-prepared SnS/MoS<sub>2</sub>/C electrode for the first three cycles at

a current density of 0.1 A g<sup>-1</sup>. For the first cycle, it delivers a discharge capacity of 1249.4 mA h g<sup>-1</sup> and obtains a reversible capacity of 1126.3 mA h g<sup>-1</sup> with a high initial coulombic efficiency of 90.2%. The value is higher than the most of other recently reported composites, as listed in Table S1.† The following two cycles show a similar capacity with the almost overlapped files. The electrode reactions can be illustrated in the CV curves, as shown in Fig. 5D. In the first anodic scan, the irreversible peaks at about 0.39 and 1.16 V are attributed to the formation of a solid electrolyte interface (SEI) on the material surface. The peaks at 0.1 and 0.8 V are attributed to the formation of Li<sub>x</sub>Sn alloys,<sup>15</sup> and another peak at 0.21 V corresponds to the conversion reaction of Mo<sup>4+</sup> to Mo<sup>0</sup>, accompanying with the formation of Li<sub>2</sub>S, and a series of peaks at 1.45 and 2.4 V are assigned to the partial oxidation of Mo to form MoS<sub>2</sub>, and the extraction of Li<sup>+</sup> by the oxidation of Li<sub>2</sub>S, respectively.<sup>48</sup> Moreover the anodic peak at 1.8 V and the cathodic peak at 1.3 V were aroused from the reversibly reaction of Li<sub>x</sub>Sns.<sup>13</sup> The overlapped curves of the second and third cycles consistent with the charge/discharge profiles revealed good reversibility. After the 250<sup>th</sup> cycle, the capacity increased to 790.1 mA h g<sup>-1</sup> due to gradually activated reactive sites. However, the MoS<sub>2</sub>/C sample in Fig. 5B shows an ICE of 84.1%, which is less than that of SnS/MoS<sub>2</sub>/C. The lost reversible capacity can be attributed to the continuous growth of SEI revealed by the always existing peaks in each anodic scan, as

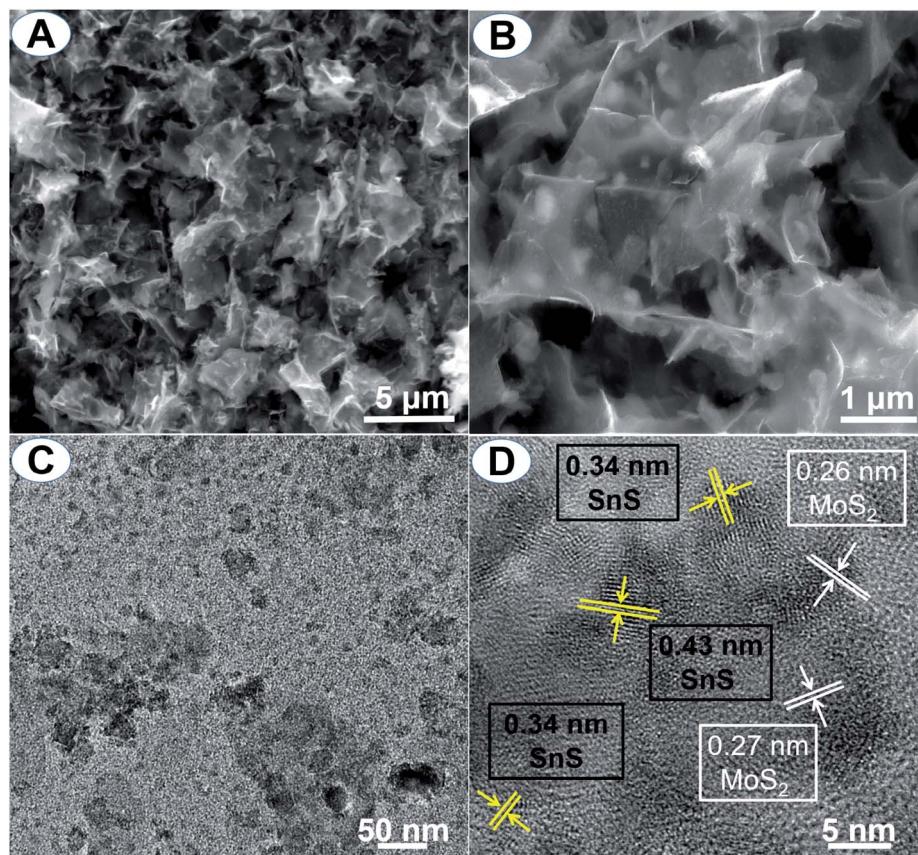


Fig. 4 SEM (A and B), TEM (C) and HRTEM (D) images of the SnS/MoS<sub>2</sub>/C composite.

shown in Fig. 5E. Although the composite structure of MoS<sub>2</sub> with the carbon matrix is closed to the binary metal sulfides, the single phase tends to produce new crystal boundaries from the

collapse of the layered structure by the large volume change. Then, the CV curve of SnS/C did not show severe SEI growing (Fig. 5F), but the lowest ICE of only 64.1% owing to the

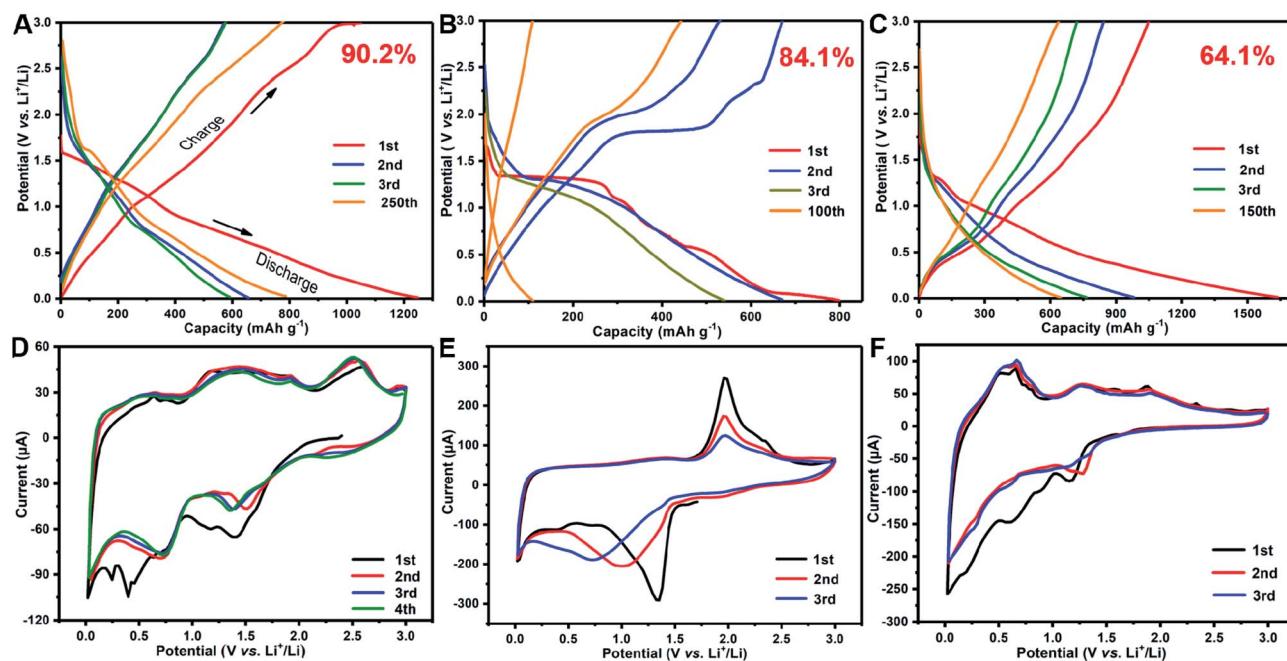


Fig. 5 The discharge/charge profiles and CV curves of the SnS/MoS<sub>2</sub>/C (A, D), MoS<sub>2</sub>/C (B, E) and SnS/C (C, F) samples.



coarsening of Sn phases led to the limited conversion back into  $\text{SnO}_2$  during Li extraction, and the reversible capacity decreased with the increase in the cycling numbers (in Fig. 5C).

Fig. 6A displays the rate capability and cycling performances of the  $\text{SnS}/\text{MoS}_2/\text{C}$  sample as an anode material in a lithium-ion battery at different current densities. Benefiting from the synergistic effects and catalytic action of Mo on the reversibility of conversion reactions, the  $\text{SnS}/\text{MoS}_2/\text{C}$  composite exhibited the highest capacity among the three samples. The average discharge capacity achieved  $651.8$  and  $238.8 \text{ mA h g}^{-1}$  at  $0.2$  and  $5 \text{ A g}^{-1}$ , respectively, as shown in Fig. 6B. As the current density returns to  $0.2 \text{ A g}^{-1}$ , the reversible capacity comes back to  $612.9 \text{ mA h g}^{-1}$ , corresponding to a retention of  $94\%$ . Compared to  $\text{SnS}/\text{MoS}_2/\text{C}$ , the  $\text{MoS}_2/\text{C}$  sample shows the lowest rate capability.  $\text{SnS}/\text{C}$  showed a comparable capability, but it had only a little capacity at a high current density of  $5 \text{ A g}^{-1}$ . At

a constant current of  $0.5 \text{ A g}^{-1}$ , the capacity of  $\text{SnS}/\text{MoS}_2/\text{C}$  remained  $726.8 \text{ mA h g}^{-1}$  after  $100$  cycles on an upward trend due to the increase in the number of active sites during cycling.<sup>14</sup> Benefited from its own structure advantage,  $\text{SnS}$  embedded dispersedly in the carbon framework also showed a good capacity retention of  $558.9 \text{ mA h g}^{-1}$ . However,  $\text{MoS}_2/\text{C}$  only delivered a specific capacity of  $115.8 \text{ mA h g}^{-1}$  after  $100$  cycles at the same current density. The lowest capacity was mainly caused by the rapid decay at the beginning cycles. The ion diffusion coefficients have been calculated from the EIS results to analyze the improved kinetic properties of charge transferring in the electrodes, as shown in Fig. 6C and D.

$D_{\text{Li}^+}$  was calculated from the follow equation:

$$D_{\text{Li}^+} = R^2 T^2 / 2 A^2 n^4 F^4 C^2 \sigma^2,$$

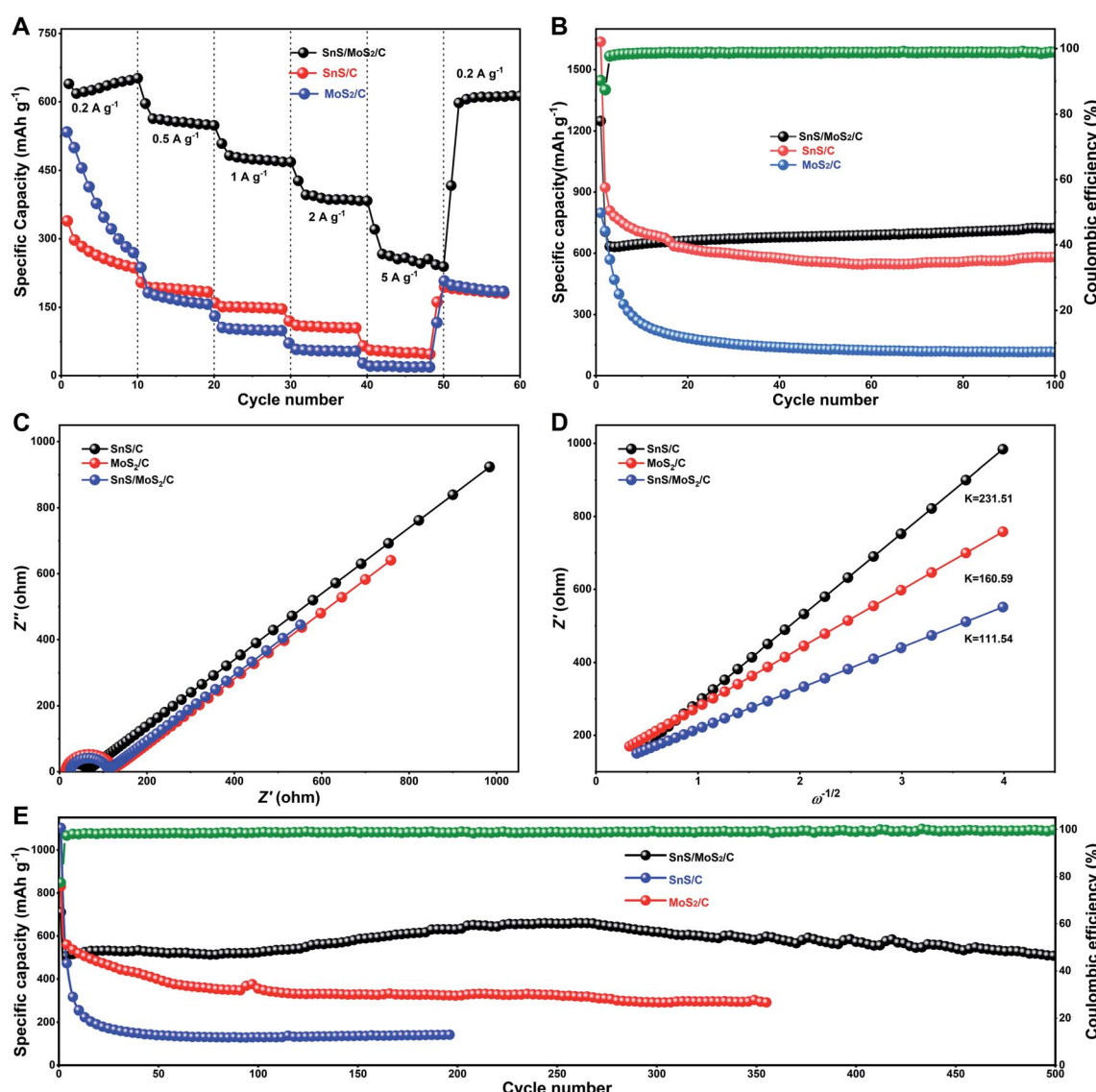


Fig. 6 Rate capability (A), short cycling capability at  $0.2 \text{ A g}^{-1}$  (B), Nyquist plots (C) and Warburg impedance coefficients (D) after  $100$  cycles, and long-term cycling performance at  $1.0 \text{ A g}^{-1}$  (E) of the  $\text{SnS}/\text{MoS}_2/\text{C}$ ,  $\text{SnS}/\text{C}$  and  $\text{MoS}_2/\text{C}$  composites.



where  $R$ ,  $T$ ,  $A$ ,  $n$ ,  $F$ , and  $C$  refer to the gas constant, temperature, surface area, electron number, Faraday constant, and sodium ion concentration, respectively. The slope of all electrodes after the 100<sup>th</sup> cycle was calculated by plotting the lines between  $Z'$  and  $\omega^{-1/2}$  to obtain  $\sigma$  for calculating the diffusion coefficient. The  $D_{Li^+}$  values of SnS/C, MoS<sub>2</sub>/C and SnS/MoS<sub>2</sub>/C after 100 cycles are  $1.39 \times 10^{-15}$ ,  $2.87 \times 10^{-15}$  and  $5.94 \times 10^{-15}$ . SnS/MoS<sub>2</sub>/C showed the highest  $D_{Li^+}$  value, demonstrating that the 3D grid facilitated the transferring kinetics of ions in the electrode. The TEM images after cycling have been provided as direct evidence to prove that the coarsening of grains is suppressed. Compared to the samples before cycling, the SnS/MoS<sub>2</sub>/C sample maintained a better pristine structure, while the SnS/C particles were broken of the bigger ones, and the grains were coarsened, as shown in Fig. S4.† In case of a closed proportion of MoS<sub>2</sub> with carbon in the SnS/MoS<sub>2</sub>/C and the MoS<sub>2</sub>/C samples, respectively, it can be revealed that the nanostructural hybrids of the SnS and MoS<sub>2</sub> play a synergy effect upon the cycling stability. Furthermore, SnS/MoS<sub>2</sub>/C also exhibits an excellent long-term cycling performance for 500 times under a higher current density of  $1.0 \text{ A g}^{-1}$  and showed a capacity of  $514.5 \text{ mA h g}^{-1}$ , as shown in Fig. 6E.

## 4. Conclusions

In summary, a binary metal–sulfide of SnS/MoS<sub>2</sub> was synthesized *via* a salt-assisted ball milling process. The heterostructure of metal sulfides interpenetrated in a conductive carbon architecture matrix, and mutually impeded the coarsening of metal grains during cycling. With the synergistic effects, the as-prepared SnS/MoS<sub>2</sub>/C composite exhibited a high ICE of 90.2% and a superior capacity retention. The improved ICE and facile synthetic strategy are expected to offer a solution for the reversibility issues of metal sulfides as well as other conversion-type anode materials for high energy LIBs.

## Conflicts of interest

There are no conflicts to declare.

## Acknowledgements

This work was supported by the National Natural Science Foundation of China (51964013 and 22002025), the Natural Science Foundation of Guangxi (2020GXNSFAA159087), the Special Fund for Guangxi Distinguished Expert, Guangxi Innovation Driven Development Subject (GUIKE AA19182020, GUIKE AA19254004), the Guangxi Technology Base and Talent Subject (GUIKE AD18126001), the Innovation Driven Key Subject of Hezhou (HEKECHUANG CX1907001) and the Basic Ability Improvement Program for Young and Middle-Age Teachers of High School in Guangxi (2019KY0709).

## References

- 1 X. Li, P. Yan, X. Xiao, J. H. Woo, C. Wang, J. Liu and J.-G. Zhang, *Energy Environ. Sci.*, 2017, **10**, 1427.
- 2 H. Wang, J. Fu, C. Wang, J. Wang, A. Yang, C. Li, Q. Sun, Y. Cui and H. Li, *Energy Environ. Sci.*, 2020, **13**, 848.
- 3 P. Li, J.-Y. Hwang and Y.-K. Sun, *ACS Nano*, 2019, **13**, 2624.
- 4 X. Li, J. Liu, L. Ouyang, B. Yuan, L. Yang and M. Zhu, *Appl. Surf. Sci.*, 2018, **436**, 912.
- 5 Y. Sun, H.-W. Lee, G. Zheng, Z. W. She, J. Sun, Y. Li and Y. Cui, *Nano Lett.*, 2016, **16**, 1497.
- 6 Q. Zhang, H. Chen, L. Luo, B. Zhao, H. Luo, X. Han, J. Wang, C. Wang, Y. Yang and Z. T. M. Liu, *Energy Environ. Sci.*, 2018, **11**, 669.
- 7 W. Li, X. Li, J. Liao, B. Zhao, L. Zhang, L. Huang, G. Liu, Z. Guo and M. Liu, *Energy Environ. Sci.*, 2019, **12**, 2286.
- 8 W. Chen, K. Song, L. Mi, X. Feng, J. Zhang, S. Cui and C. Liu, *J. Mater. Chem. A*, 2017, **5**, 10027.
- 9 A. K. Thakur, M. S. Ahmed, G. Oh, H. Kang, Y. Jeong, R. Prabakaran, M. P. Vikram, S. W. Sharshir, J. Kim and J.-Y. Hwang, *J. Mater. Chem. A*, 2021, **9**, 2628–2661.
- 10 L. Lin, X. Xu, C. Chu, M. K. Majed and J. Yang, *Angew. Chem., Int. Ed.*, 2016, **55**, 14063.
- 11 R. Hu, W. Sun, Y. Chen, M. Zeng and M. Zhu, *J. Mater. Chem. A*, 2014, **2**, 9118.
- 12 T. Liang, R. Hu, H. Zhang, H. Wang, Y. Ouyang, J. Liu, L. Yang and M. Zhu, *J. Mater. Chem. A*, 2018, **6**, 7206.
- 13 D. D. Lecce, R. Verrelli, D. Campanella, V. Marangon and J. Hassoun, *ChemSusChem*, 2017, **10**, 1607.
- 14 Y. He, L. Xu, C. Li, X. Chen and X. Jiao, *Nano Res.*, 2018, **11**, 3555.
- 15 X. W. Guo, X. P. Fang, Y. Sun, L. Y. Shen, Z. X. Wang and L. Q. Chen, *J. Power Sources*, 2013, **226**, 75.
- 16 R. Jia, J. Yue, Q. Xia, J. Xu, X. Zhu, S. Sun, T. Zhai and H. Xia, *Energy Storage Mater.*, 2018, **13**, 303.
- 17 C.-Y. Wu, H. Yang, C.-Y. Wu and J.-G. Duh, *J. Alloys Compd.*, 2018, **750**, 23.
- 18 J. Shi, Y. Wang, Q. Su, F. Cheng, X. Kong, J. Lin, T. Zhu, S. Liang and A. Pan, *Chem. Eng. J.*, 2018, **353**, 606.
- 19 P. Zheng, Z. Dai, Y. Zhang, K. N. Dinh, Y. Zheng, H. S. Fan, J. Yang, R. Dangol, B. Li, Y. Zong, Q. Yan and X. Liu, *Nanoscale*, 2017, **9**, 14820.
- 20 Y. Huang, Y. Wang, X. Zhang, F. Lai, Y. Sun, Q. Li and H. Wang, *Mater. Lett.*, 2019, **243**, 84.
- 21 Q. Pan, F. Zheng, Y. Wu, X. Ou, C. Yang, X. Xiong and M. Liu, *J. Mater. Chem. A*, 2018, **6**, 592.
- 22 L. Cui, C. Tan, G. Yang, Y. Li, Q. Pan, M. Zhang, Z. Chen, F. Zheng, H. Wang and Q. Li, *J. Mater. Chem. A*, 2020, **8**, 22593.
- 23 J. Zhu, X. Zhang, C. Zeng, A. Liu and G. Hu, *Mater. Lett.*, 2017, **209**, 338.
- 24 X. Hu, J. Chen, G. Zeng, J. Jia, P. Cai, G. Chai and Z. Wen, *J. Mater. Chem. A*, 2017, **5**, 23460.
- 25 Y. Wang, W. Kang, P. Ma, D. Cao, D. Cao, Z. Kang and D. Sun, *Mater. Chem. Front.*, 2020, **4**, 1212.
- 26 P. Xue, N. Wang, Y. Wang, Y. Zhang, Y. Liu, B. Tang, Z. Bai and S. Dou, *Carbon*, 2018, **134**, 222.
- 27 Y. Zhang, Z. Ma, D. Liu, S. Dou, J. Ma, M. Zhang, Z. Guo, R. Chen and S. Wang, *J. Mater. Chem. A*, 2017, **5**, 512.



28 D. H. Youn, S. K. Stauffer, P. Xiao, H. Park, Y. Nam, A. Dolocan, G. Henkelman, A. Heller and C. B. Mullins, *ACS Nano*, 2016, **10**, 10778.

29 J. Liu, M. Gu, L. Ouyang, H. Wang, L. Yang and M. Zhu, *ACS Appl. Mater. Interfaces*, 2016, **8**, 8502.

30 C. Li, B. Wang, D. Chen, L.-Y. Gan, Y. Feng, Y. Zhang, Y. Yang, H. Geng, X. Rui and Y. Yu, *ACS Nano*, 2020, **14**, 531.

31 Y. Cheng, Z. Wang, L. Chang, S. Wang, Q. Sun, Z. Yi and L. Wang, *ACS Appl. Mater. Interfaces*, 2020, **12**, 25786.

32 J. Cai, Z. Li and P. K. Shen, *ACS Appl. Mater. Interfaces*, 2012, **4**, 4093.

33 S. Zhang, H. Ying, P. Huang, J. Wang, Z. Zhang, T. Yang and W. Han, *ACS Nano*, 2020, **14**, 17665.

34 X. Xiong, C. Yang, G. Wang, Y. Lin, X. Ou, J.-H. Wang, B. Zhao, M. Liu, Z. Lin and K. Huang, *Energy Environ. Sci.*, 2017, **10**, 1757–1763.

35 H. Fang, Y. Chen, M. Wen, Q. Wu and Q. Zhu, *Nano Res.*, 2017, **10**, 3929.

36 Q. Pan, F. Zheng, Y. Wu, X. Ou, C. Yang, X. Xiong and M. Liu, *J. Mater. Chem. A*, 2018, **6**, 592.

37 S. Chen, K. Xing, J. Wen, M. Wen, Q. Wu and Y. Cui, *J. Mater. Chem. A*, 2018, **6**, 7631.

38 H. Wang, Q. Pan, Q. Wu, X. Zhang, Y. Huang, Q. Li and X. Sun, *J. Mater. Chem. A*, 2017, **5**, 4576.

39 Q. Pan, Y. Huang, H. Wang, G. Yang, L. Wang, J. Chen, Y. Zan and Q. Li, *Electrochim. Acta*, 2016, **197**, 50.

40 C. Zhang, Z. Lin, Z. Yang, Z. D. Xiao, P. Hu, H. Xu, Y. Duan, S. Pang, L. Gu and G. Cui, *Chem. Mater.*, 2015, **27**, 2189–2194.

41 Y. Wang, S. Luo, M. Chen and L. Wu, *Adv. Funct. Mater.*, 2020, **30**, 2000373.

42 L. Zhang, J. Song, Y. Liu, X. Yuan and S. Guo, *J. Power Sources*, 2018, **379**, 68.

43 R. Hu, Y. Ouyang, T. Liang, H. Wang, J. Liu, J. Chen, C. Yang, L. Yang and M. Zhu, *Adv. Mater.*, 2017, **29**, 1605006.

44 Z. Huang, S. Ding, P. Li, C. Chen and M. Zhang, *Nanotechnology*, 2020, **32**, 025401.

45 R. Hu, Y. Ouyang, T. Liang, X. Tang, B. Yuan, J. Liu, L. Zhang, L. Yang and M. Zhu, *Energy Environ. Sci.*, 2017, **10**, 2017.

46 Y. Chao, R. Jalili, Y. Ge, C. Wang, T. Zheng, K. Shu and G. G. Wallace, *Adv. Funct. Mater.*, 2017, **27**, 1700234.

47 L. Zhang and X. W. Lou, *Chem.-Eur. J.*, 2014, **20**, 5219.

48 Y. Jiao, A. Mukhopadhyay, Y. Ma, L. Yang, A. M. Hafez and H. Zhu, *Adv. Energy Mater.*, 2018, **8**, 1702779.

